Characterizing turbulent structures in the atmospheric boundary layer with super-large-scale particle image velocimetry

Michael Heisel[1,*], Teja Dasari[1], Alec Petersen[1], Yun Liu[2], Jiarong Hong[1], Filippo Coletti[1], Michele Guala[1]

1: St. Anthony Falls Laboratory, The University of Minnesota, USA
2: Dept. of Mechanical and Civil Engineering, Purdue University Northwest, USA
* Correspondent author: heise070@umn.edu

Keywords: Field-scale PIV, Turbulent boundary layers, Ramp-like structures

ABSTRACT

Super-large-scale particle image velocimetry (SLPIV) using natural snowfall has previously been shown to be a reliable field measurement technique for near-surface atmospheric flows (Toloui et al *Exp Fluids* 2014, 55:1737; Hong et al *Nat Comm* 2014, 5:4216). Here we present results from SLPIV measurements in the thermally neutral atmospheric surface layer. The data were collected at the EOLOS field station over relatively flat, snow-covered farmland, allowing the development of a fully rough wall boundary layer with a Reynolds number $Re_\tau = O(10^6)$. The data include three 15-minute acquisition periods with a field of view extending from 3 m to 19 m above the ground. The field captures the top of the roughness sublayer and the bottom of the extensive logarithmic region. The flow statistics are validated and supplemented by sonic anemometry from a meteorological tower immediately downstream of the SLPIV field of view. The SLPIV resolution is sufficient for resolving coherent structures temporally and spatially. The planar measurements therefore provide temporal and spatial characterization of key wall turbulence features at high Reynolds number, including ramp-like structures, spanwise vortices, and uniform momentum zones. We present the temporal tracking of spanwise vortices as a demonstration of the possible analyses afforded by the dataset. In comparing the findings to laboratory studies, Reynolds number similarity and the scaling behavior of characteristic properties are discussed.

1. Introduction

Large-scale boundary layer flows are ubiquitous in natural and engineered systems. Laboratory facilities are continually improving in terms of scale and measurement techniques in order to represent and study these flows. However, the scale of laboratory boundary layers is still orders of magnitude below many geophysical scales such as atmospheric surface layers. There are field facilities such as SLTEST in Utah which provide arrayed point measurements at the atmospheric scale, but the lack of spatial resolution prevents the study of turbulent structures in truly high Reynolds number flow. Recent studies at the EOLOS field facility in Minnesota have validated the use of snow particles as tracers for super-large-scale particle image velocimetry (SLPIV) (Toloui et

al 2014; Hong et al 2014). Here, we employ the same SLPIV technique using snow particles to measure velocities in the atmospheric surface layer with high spatial resolution relative to other field facilities.

2. Methodology

The experimental setup for the facility is shown in Figure 1. The inset picture shows the searchlight and concave mirror used to reflect a sheet of light upward to illuminate the snow particles. The sheet was oriented along the wind direction to mitigate out-of-plane motion. The illuminated particles were captured using 30 Hz video by a camera offset from the light sheet. Standard cross-correlation PIV was conducted on the video frames using in-house code (Nemes et al 2015), providing a field of view extending from $z = 2$ to 18 m with spatial resolution $\Delta x \approx$ 0.27 m and temporal resolution $\Delta t = 0.03$ s. PIV measurements are supplemented by sonic anemometer measurements on a meteorological (met) tower 17 m downstream of the imaging field. Measurements were taken for three 15-minute periods.
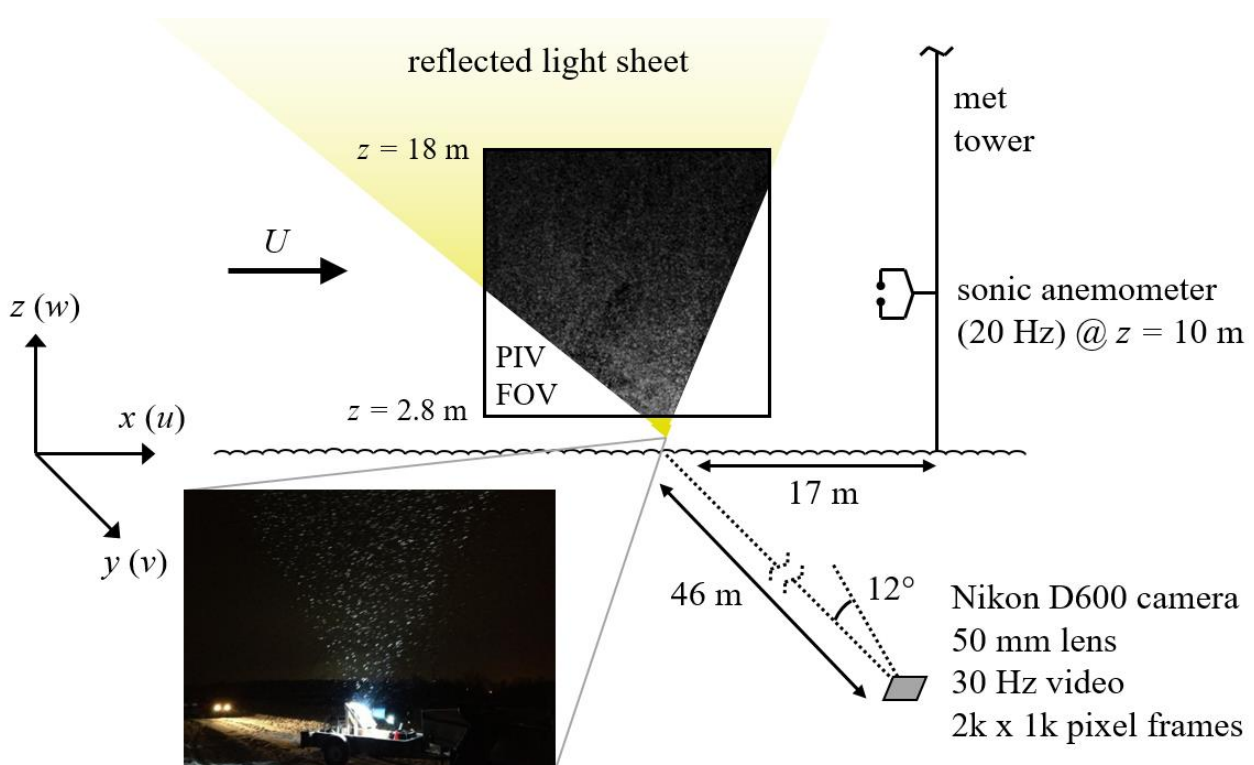

Fig. 1 Schematic of the field experiment. The offset camera captures video of the snow particles illuminated by the reflected light sheet resulting in the field of view (FOV) shown. The light sheet is created by a searchlight projection reflected from a concave mirror (inset image). The met tower provide sonic and cup and vane anemometer measurements up to $z = 128$ m.

We assessed the thermal stability for the three periods using the Monin-Obukhov ratio $\zeta = z/L$, where L is the Obukhov length defined using sonic anemometer measurements at $z = 10$ m. The resulting ratio was $\zeta < 0.01$ for each period, indicating near-neutral thermal stratification for which buoyancy effects can be considered negligible.

Using digital in-line holography on a sample of almost 200 snow particles (see Nemes et al 2017), we identified the snow particles as individual ice crystals in the form of hexagonal plates with average diameter $D_p = 0.6$ mm and thickness $H_p = 0.3$ mm. Following the model of Thompson et al (2008), we estimated the particle density to be $\rho_p = 210$ kg m^{-3}. We then estimated the particle response time τ_p using the Stokes drag approximation corrected for finite particle Reynolds number: $\tau_p = \rho_p D_p{}^2/18\mu(1 + 0.15Re_p{}^{0.687})$ where $Re_p = W_p D_p/\nu$ is the particle Reynolds number (Crowe et al 1998). In the above expressions, μ and ν are the dynamic and kinematic viscosities of air, respectively, and $W_p = 1.3$ m s^{-1} is the average particle settling velocity measured by the SLPIV. The resulting particle response time, $\tau_p = 0.074$ s, is likely conservative by at least a factor of two based on observations by Nemes et al (2017). The limiting flow time scale of the SLPIV measurements is $\tau_f = l/u_{rms} = 0.9$ s, where $l = 0.54$ m is the interrogation window size and $u_{rms} = 0.6$ m s^{-1} is the maximum measured root-mean-square (rms) velocity. The particle Stokes number relevant to the SLPIV measurements is therefore $St = \tau_p/\tau_f = 0.08$. Considering the value is a conservative estimate, the snow particles are reasonable flow tracers for this experiment. A more in-depth investigation on possible bias effects due to the snowflake inertia is warranted, but is outside the scope of this paper. The inertia manifests itself in the results through an appreciable settling velocity W_p.
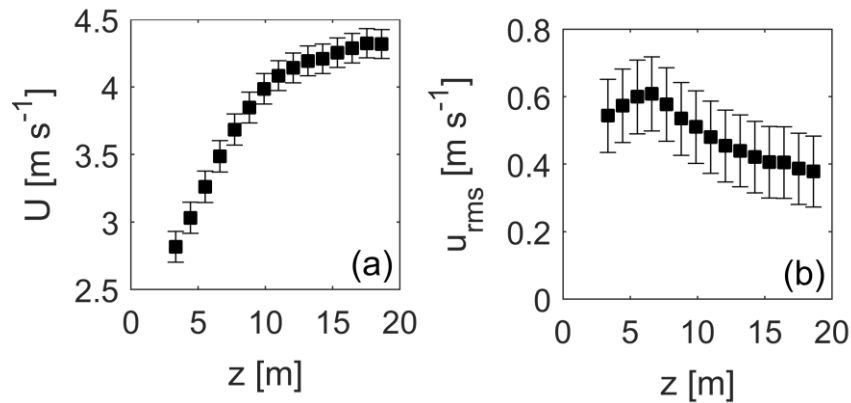

Fig. 2 Estimated experimental uncertainties for wall-normal profiles of the first SLPIV data set: (a) mean velocity; (b) streamwise root-mean-squared velocity. Every fourth data point is shown for clarity.
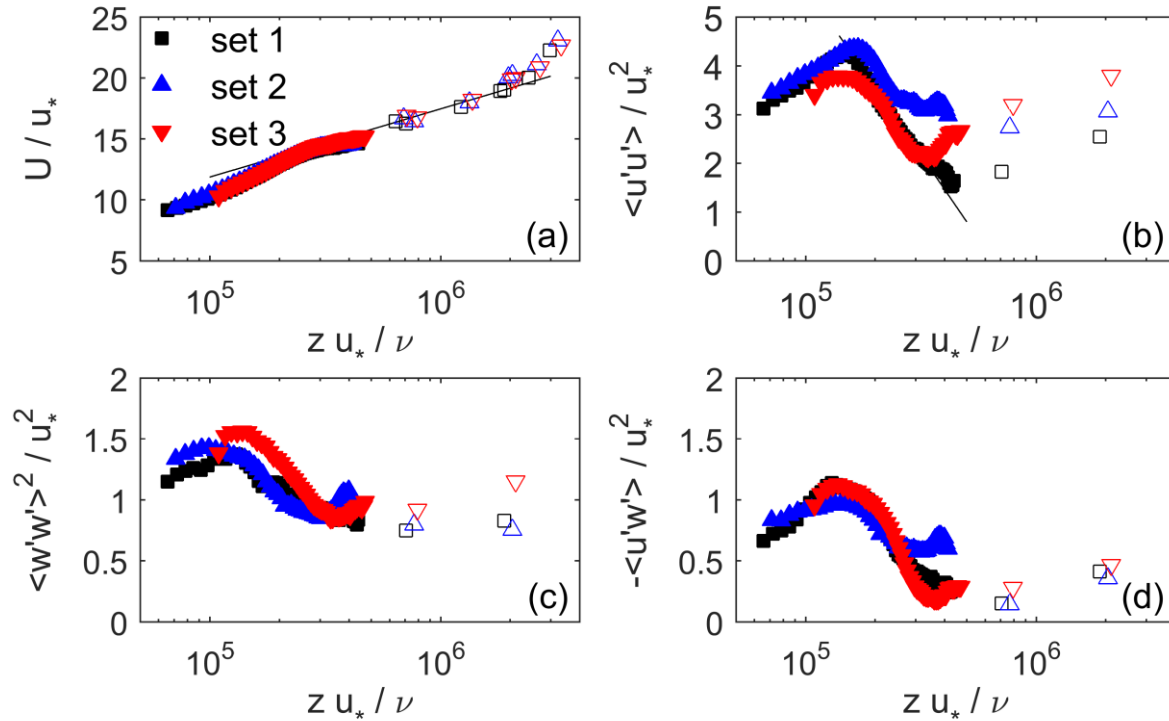
Fig. 3 Velocity profiles for the three SLPIV data sets normalized using inner wall units: (a) mean velocity including the log law fit (black line); (b) streamwise variance; (c) wall-normal variance; (d) Reynolds shear stress. SLPIV data (closed symbols) are supplemented by met tower data (open symbols).

3. Results

The velocity profiles are summarized in Figures 2 and 3. Figure 2 provides the estimated total uncertainty of the measurements for the first data set. For the streamwise u and vertical w velocity components, fluctuations were calculated using the standard Reynolds decomposition by subtracting the height-dependent mean (streamwise and settling) velocity. The profiles in Figure 3 are normalized using inner wall units, and show good agreement with the literature. Met tower measurements are included to extend the range of the profiles. The mean velocity in Figure 3a follows a log-linear increase from $z = 5.5$ to 70 m and the streamwise velocity in Figure 3b shows a log-linear decrease expected in the logarithmic region (see e.g., Marusic et al 2013). The peaks in the wall-normal variance ($\langle w'w' \rangle^+ \approx 1.5$ in Figure 3c) and Reynolds shear stress ($-\langle u'w' \rangle^+ \approx 1$ in Figure 3d) match well with previous atmospheric measurements (see e.g., Kunkel and Marusic 2006). The fully rough conditions are confirmed by the roughness function $\Delta U^+ = 22$ m s^{-1}, corresponding to equivalent sandgrain roughness $k_s = 1.2$ m and aerodynamic roughness length $z_o = 0.04$ m. The profile trends in the region $z^+ < 2 \times 10^5$ are inferred to be influenced by wall roughness effects and within the roughness sublayer, and values above this limit are considered

be a canonical logarithmic region. The three data sets were used to parameterize the boundary layer, but later results focus on the first data set.

A key feature of boundary layers studied at the lab-scale is ramp-like structures. The statistical persistence of these structures is evident from the inclination of the streamwise velocity fluctuation two-point correlation map. Field measurements have shown correlation inclinations near the wall (Hutchins et al 2012). Our data reveal ramp-like structures both in instantaneous vector fields (Figure 4a) and the inclined two-point correlation (Figure 4b), indicating the presence of these structures for fully rough boundary layers. In addition to supporting the apparent universal existence of ramp-like structures in canonical boundary layers, the presence of the structures in our range of heights also suggests the structures scale in size with an intermediate or outer scale rather than inner wall units (which would not result in inclined structures extending into our field of view).

The remaining results presented here relate to the tracking of spanwise vortices in time. We identified vortices using the swirling strength λ_{ci}, where the sign of the swirling strength is determined by the sign of the out-of-plane vorticity ω_y. The high-pass cutoff threshold value was $\lambda_{min} = 0.05 \times \max(\lambda_{ci})$, i.e. 5% of the maximum, which is in a range consistent with Ganipathisubramani et al (2006). To track persistent vortex events, contiguous regions above the threshold in the spatio-temporal domain were recorded if the region extended for at least 8 SLPIV frames, i.e. 0.25 s. An isosurface plot resulting from the tracking procedure is shown in Figure 5.
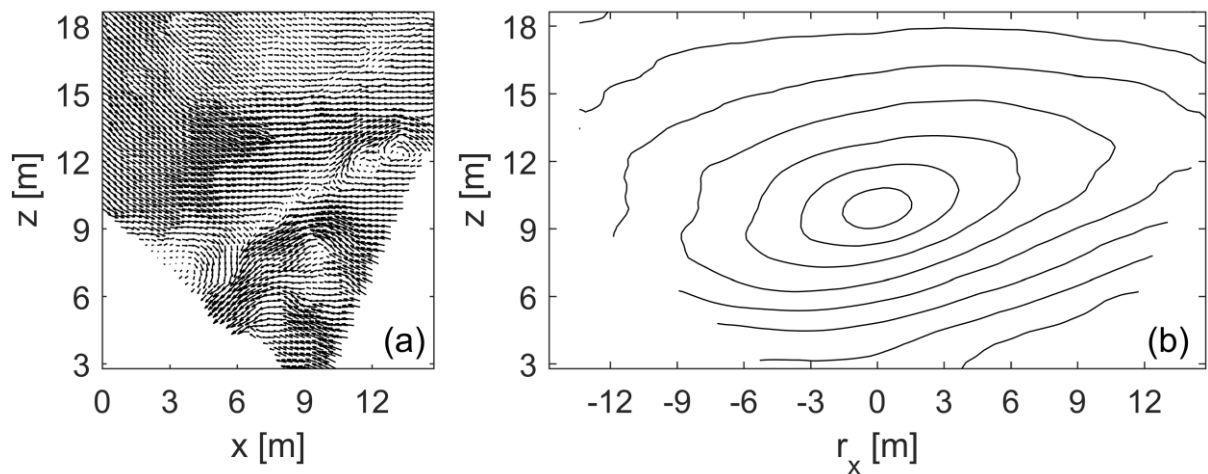

Fig. 4 Evidence of ramp-like structures: (a) instantaneous velocity vector field with subtracted convective velocities $U_c = 3.75$ m s^{-1} and $W_c = -1$ m s^{-1}; (b) contours of the streamwise velocity fluctuation two-point correlation ρ_{uu} for the reference height $z_{ref} = 10$ m.
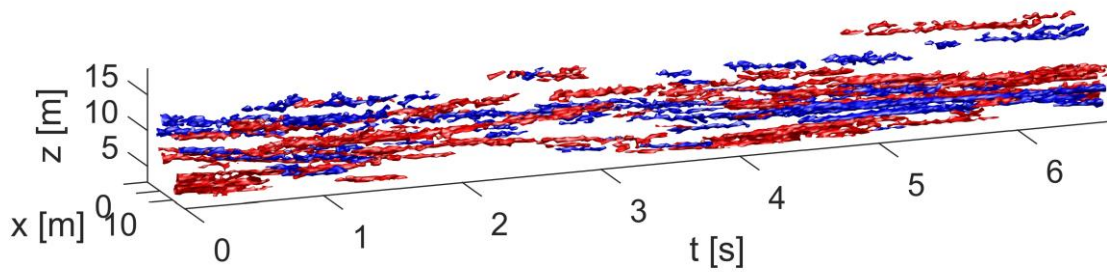
Fig. 5 Isosurfaces of the swirling strength threshold value $\lambda_{min} = 5\%$ for tracked vortex events. Red surfaces correspond to prograde vortices (with negative swirling strength based on the vorticity sign) and blue surfaces correspond to retrograde vortices.

For each frame in an event, the vortex has an area given by contours of the threshold λ_{min}. The vortex center is calculated as the geometric centroid of the area weighted by the swirling strength values. The vortex area and center are demonstrated in Figure 6a. The convective velocity of the eddy was calculated by two methods: (i) a linear fit of the vortex centroid across frames and (ii) the average velocity of the vectors in the vortex event. Figure 6b shows a probability distribution of the vortex convective velocity U_ω calculated by method (i) relative to the time-average mean velocity $U(z)$ at the height of the vortex z_ω. The mode of the distribution is close to 1 and the average values for methods (i) and (ii) are both $\langle U_\omega / U(z_\omega) \rangle = 1 \pm 0.01$. Treating the prograde and
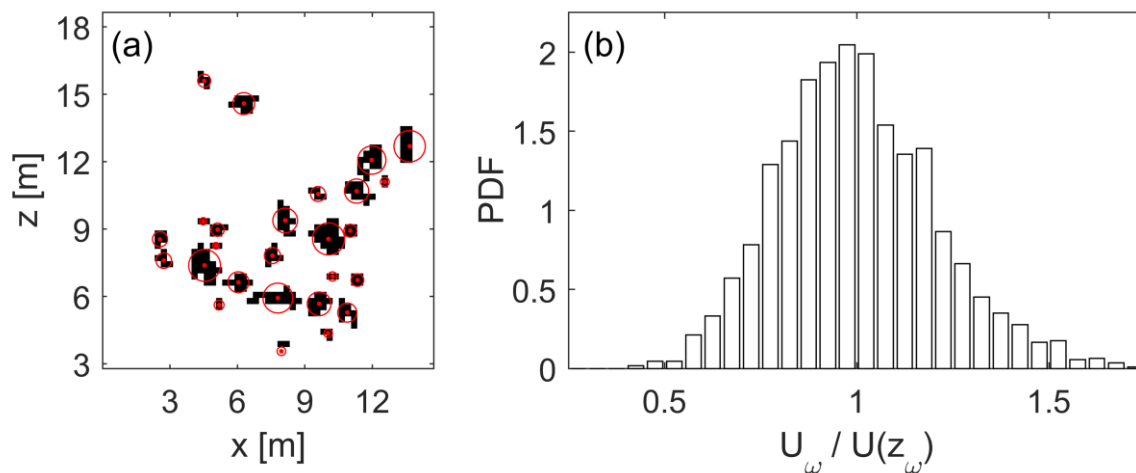

Fig. 6 (a) demonstration of vortex parameterization using the same SLPIV frame as Figure 4a. The area and weighted centroid (red dot) are determined for each group of vectors (black squares) above the swirling strength threshold λ_{min}. The red circles have the same area as the vortex in the frame. (b) probability distribution of vortex convective velocities U_ω relative to the time-averaged mean velocity at the height of the vortex z_ω.

retrograde vortices separately yielded similar results. The vortices are therefore convected at the same rate as the mean flow.

Similar to method (ii) in the previous paragraph, the standard deviation σ_ω can be calculated for the streamwise velocity vectors in the vortex event. The average standard deviation is $\langle \sigma_\omega \rangle = 0.18$ m s^{-1}, less than half the time-average standard deviation (see Figure 2c). While some deviation in the velocity is induced by rotation, the vortices are indeed coherent regions within the turbulent flow.

Using the vortex area, the characteristic size can be determined assuming the vortex is circular. The effective radius of the vortex in each frame is $R_{eff} = (A_\omega/\pi)^{1/2}$ and the effective diameter D_{eff} is twice the radius. To assess the circularity of the shape, the shape factor S is defined as the ratio of points within R_{eff} of the vortex center to the total number of points. Figure 7a shows the average shape factor $\langle S \rangle$ for multiple ranges of calculated diameters D_{eff}. The vortices are reasonably circular at all sizes, indicating diameter D_{eff} is representative as a characteristic size. Figure 7b shows separate probability distributions of the effective diameter for prograde and retrograde vortices. The average size is $D_{eff} = 0.76$ m for prograde vortices and $D_{eff} = 0.63$ m for retrograde vortices. The average size is weakly sensitive to the choice of threshold λ_{min}, ranging from $D_{eff} = 0.6$ to 0.8 m in the threshold range $\lambda_{min} = 2$ to 20%. General conclusions drawn from the results are unaffected by the threshold.
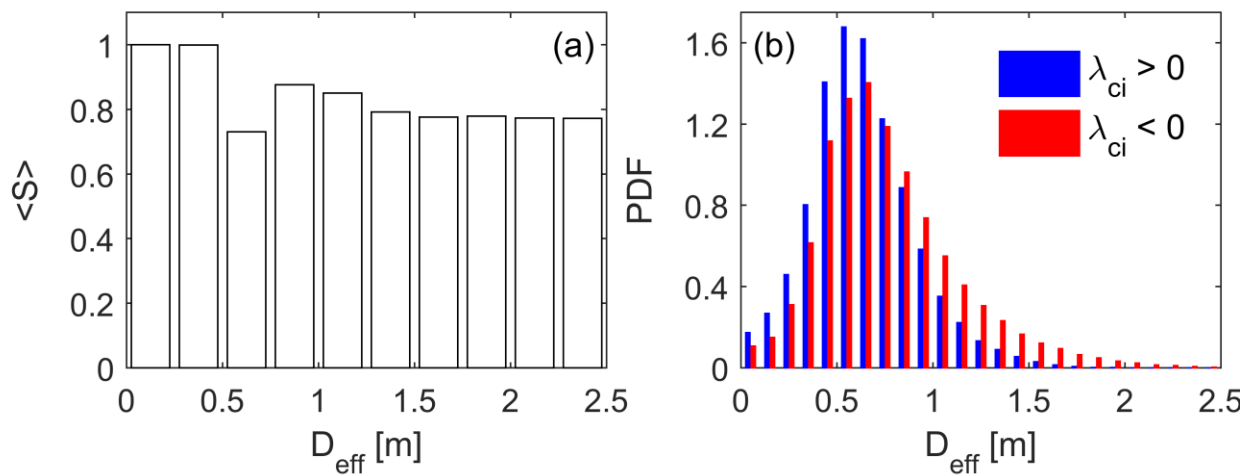

Fig. 6 Effective diameter of the tracked vortices: (a) average shape factor $\langle S \rangle$ for binned ranges of effective diameter D_{eff}; (b) probability distributions of D_{eff} for prograde and retrograde vortices.

4. Conclusion

We demonstrate that SLPIV can accurately measure first- and second-order flow statistics across an extended elevation range. The SLPIV technique is not limited to the field of view employed here; a more recent field deployment measured up to $z = 140$ m. SLPIV can also be used study the structure of high Reynolds number wall turbulence in the atmospheric surface layer, both in terms of coherent motions and individual energetic vortices. We plan to extend the analysis to the zones of uniform momentum and to discuss in more depth the scaling parameters required to compare our results with wind tunnel data at lower Reynolds number.

5. References

Crowe CT, Schwarzkopf JD, Sommerfeld M, and Y Tsuji (1998). Multiphase Flows with Droplets and Particles. CRC Press.

Ganipathisubramani B, Longmire E, and I Marusic (2006). Experimental investigation of vortex properties in a turbulent boundary layer. Phys Fluids, 18.

Hong J, Toloui M, Chamorro LP, Guala M, Howard KB, Riley S, Tucker J, and F Sotiropoulos (2014). Natural snowfall reveals large-scale flow structures in the wake of a 2.5-MW wind turbine. Nat Comm, 5:4216.

Hutchins N, Chauhan K, Marusic I, Monty J, and J Klewicki (2012). Towards reconciling the large-scale structure of turbulent boundary layers in the atmosphere and laboratory. Boundary-Layer Meteorol, 145.

Kunkel GJ and I Marusic (2006). Study of the near-wall-turbulent region of the high-Reynolds-number boundary layer using an atmospheric flow. J Fluid Mech, 548.

Marusic I, Monty JP, Hultmark M, and AJ Smits (2013). On the logarithmic region in wall turbulence. J Fluid Mech, 716(R3):

Nemes A, Dasari T, Hong J, Guala M, and F Coletti (2017). Snowflakes in the atmospheric surface layer: observation of particle–turbulence dynamics. J Fluid Mech, 814.

Thompson G, Field PR, Rasmussen, RM, and WD Hall (2008). Explicit forecasts of winter precipitation using an improved bulk microphysics scheme. Part II: implementation of a new snow parameterization. Mon Weath Rev, 136(12):5095.

Toloui M, Riley S, Hong J, Howard KB, Chamorro LP, Guala M, and Tucker J (2014). Measurement of atmospheric boundary layer based on super-large-scale particle image velocimetry using natural snowfall. Exp Fluids, 55:1737.